

CHAPTER 1

INTRODUCTION

1.1 Motivation

This present study is motivated from Tsa's work [1], which carried out a numerical study to investigate the counterflow diffusion flame behaviors over a single porous cylinder. He found that a lift-off flame occurs after a wake flame as the incoming flow velocity further increases, then, it jumps back in a form of wake flame again when the velocity continues to increase. The existence of a lift-off flame was verified by a corresponding experimental observation by Chang [2], who built a wind tunnel to observe the flame lift-off phenomena over a Tsuji burner and investigate the corresponding mechanism. He indicated that the lift-off flame arises because the high pressures generated at the two flame fronts depress the vortices behind the cylinder and destroy them eventually. The lift-off height becomes larger as the incoming flow velocity increases. When the height is large enough, the vortices are generated again behind the cylinder. Then, the somewhat unstable lift-off flame front is drawn back by the recirculating flow to become a wake flame again. However, no influence of flow structures, which were interacted with the combustion and vice versa, could be visually observed in the flow field due to the existence of flame. Therefore, the present work intends to develop the cold flow field visualization around and behind the cylinder or sphere burners to understand their influence on the resultant flames.

The experimental set-up basically is the same as the one used by Chang [2], except the applications of the smoke-generation wire and laser-sheet lighting which are used for the flow visualization.

1.2 Literature Review

The flame feature of lift-off phenomenon was first identified by an experimental observation of Wang [3]. However, the original goal of Wang [3] was not to investigate the existence of lift-off flame over a porous burner. Therefore, he did not explain any physical mechanism for such phenomenon. The numerical simulations and experimental investigations were carried out by Tsa [1] and Chang [2], respectively, to observe the flame lift-off phenomena and investigate the corresponding mechanism. Tsa [1] modified the original combustion model of Chen and Weng [4] by adopting the four-step chemical kinetics instead of the one-step overall kinetics. For the case of full surface fuel-ejection, when the inflow velocity exceeds 1.01 m/sec, the wake flame will lift up and transform into a lift-off flame. However, when the velocity continues to increase, the lift-off flame comes back to become a wake flame again. The maximal lift-off height is $1.3D$ when the inflow velocity is 1.01 m/sec, and this height is retained until the velocity is 1.30 m/sec. Then, gradually increasing the inflow velocity to 1.39 m/sec causes the flame lift-off height slowly to decrease until the lift-off flame is reattached to the porous cylinder. The wake flame reappears when the inflow velocity exceeds 1.39 m/sec. He also found that a larger fuel-ejection area yields a higher surviving inflow velocity of the lift-off flame. However, varying

the fuel-ejection velocity barely influences the flame lift-off height. The resultant simulations were verified by the corresponding experiments of Chang [2]. To analyze the flame behaviors, the fuel ejection velocity, covering the whole cylinder surface, is fixed at 1.23 cm/sec. The lift-off flame commences to appear as the incoming flow velocity is equal to 1.05 m/sec and the corresponding height is 2.5 mm. The maximal lift-off height is 5 mm when the velocity is 1.21 m/sec. As inflow velocity reaches 1.63 m/sec, the base of lift-off flame drops back to the cylinder again, and it becomes the second wake flame. Further increasing the inflow velocity, the lift-off flame will never show up again. Besides, he found that when the fuel ejection velocity increases to 1.4 cm/sec, the first wake flame is not observed. However, it still has the second wake flame after the lift-off flame. Wohl et al. [5] conducted the flame stability experiment over a nozzle port by changing gas velocity. They found that when the gas velocity increases at a given butane concentration, the flame position would change from the near region of port to the far one, and then the flame near port is transformed into a lifted flame. Later, the lifted flame could be drawn back to port by reducing the gas velocity below the lift-off velocity. The lift velocity at each given fuel concentration would form a lift curve. Relatively, the transition velocity curve, a transformation from a lift flame into a flame near the port, would become drop-back.

The flow behaviors past a sphere at varying Reynolds numbers have been studied by many researches. Taneda [6] used flow visualization method to study the wake behind a sphere, mounted by string. The Reynolds number for the flow was in the range of $5 < Re < 300$, in which

Re was based on the sphere diameter, D , and velocity, U . He found that separation from the sphere starts to occur at $Re \sim 24$ and results in the generation of an axisymmetric vortex ring. Regarding the stability of the resultant wake, he observed a faint periodic motion 'with a very long period' at the rear of vortex ring beginning at $Re = 130$. Natarajan and Acrivos [7] investigated the stability of the axisymmetric sphere flow using a finite-element method. They found a regular bifurcation, namely, a transition to steady flow, at $Re = 210$ and naturally suggested that this corresponds to a transition from the steady, axisymmetric wake to the steady, non-axisymmetric and double-thread wake. The regime of unsteady vortex shedding from a sphere received the most attention in the literature. The observed onset of the shedding regime covered the range of $290 < Re < 400$. Achenbach [8] and Sakamoto and Haniu [9] presented the frequency measurements for unsteady wake. As Re was close to 400 or up to 420, the onset of unsteadiness, a strongly periodic process, was identified by the observation of a single frequency in the wake at a Strouhal number (St) in the range of $0.15 < St < 0.17$. They also showed in detail the visualizations of hairpin vortices shedding from spheres. The numerical solutions of the unsteady flow past a sphere was carried out by Tomboulides et al. [10]. They recorded that the unsteady transition was in the range of $270 < Re < 285$. Johnson and Patel [11] numerically and experimentally investigated an incompressible viscous fluid flow past a sphere. Their calculations for Re up to 200 showed a steady, axisymmetric flow and they agreed well with the previous experimental observations. For Re from 210 to 270, a steady, non-axisymmetric flow was found and it was also in agreement with the previous work. Unsteady

flow was predicted at Re greater than 270. The results at a Reynolds number of 300 showed a highly organized periodic flow dominated by vortex shedding.

The investigation of the wake formation behind a circular cylinder also has received a great deal of attention. Tritton [12] carried out the experiments in both wind and water tunnels for the flow past a circular cylinder in a stream with the Reynolds number ranged from 0.5 to 100. He provided experimental evidence for where being a transition in the mode of the vortex street in the wake of a cylinder at a Reynolds number around 90. Investigations on the nature of this transition and the differences between the flows on either side of it were described. The observations suggested that the low-speed mode arises because of the instability of the wake, while in the high-speed mode the vortex street is directly affected by the walls of the cylinder. He also indicated that there are oscillations with the vortex street frequency of the attached eddy on each side of the transition Reynolds number. In the low-speed mode, the oscillations are produced through the beginnings of an instability that develops further as it goes downstream and the same fluid remains in the attached eddies throughout. Nevertheless, in the high-speed mode, a fully developed vortex street exists from its starting appearance that close to the cylinder and the fluid is continually moving into the vortex. Similarly, a detailed flow visualization study of vortex street wakes at low Reynolds number, less than 2,000, was carried out by Gerrard [13]. He divided the range of Reynolds numbers in certain regimes. When $Re < Re_{osc}$, the flow is steady with standing eddies. (Re_{osc} is the Reynolds number above which oscillations are always found.) When $Re_{osc} < Re < Re_{vs}$, the wake

behind the cylinder is wavy, and there is no accumulation of dye into vortices. When $Re_{vs} < Re < 100$, the wavy wake changes to the vortex street one, and the remnants of the standing eddies still present. When $100 < Re < 140$, the efficiency of convective mass transfer increases behind the cylinder. When $140 < Re < 500$, the vortex strength of the flow is irregular. The flow is more nearly two-dimensional one. When $350 < Re < 2,000$, there are transition waves in the separated layers and transit to turbulence in the vortex cores on formation. He found that the time taken to accelerate a vortex to its final convective velocity at $Re = 100$ is a discontinuity. Moreover, the most important is that he indicates a strong transition in the strength of the shed vortex at this Reynolds number. Zdravkovich [14] conducted the investigation on the formation of the Kármán vortex street at the Reynolds number ranged from 30 to 100 in a vertically upward low-speed wind tunnel. At this range, smoke streaklines were observed from Reynolds numbers, where the Kármán vortex street does not exist to those where it is fully developed. He indicated that the instability of the shear layers led to the initial staggered vorticity concentration when the Reynolds number was not too low. And the rolling-up process strengthened both the vorticity concentration and the circulation about the future vortex cores. He also studied the mass transfer, resulted from the newly formed vortex street, showed at first a strong interaction between the new vortices and the surrounding fluid, then, the interaction was weakened as the strength of the vortices declined. Perry et al. [15] used a variety of flow visualization techniques to investigate the vortex shedding process behind a circular cylinder. They examined the instantaneous streamline and streakline patterns of the

vortex street wake behind the cylinder. They showed that only in the time-averaged sense the classical picture in which a closed cavity behind a body is true. The closed cavity appears during the starting-up-process. However, once the vortex shedding begins, it becomes open and the instantaneous “alleyways” of fluid penetrate into the cavity. They also introduced critical points on which the slopes of the instantaneous streamlines become indeterminate. Green and Gerrard [16] utilized an optical interferometer for the visualization of the wake behind a circular cylinder at low Reynolds number. Because several experiments and numerical analyses showed that close to the cylinder the vortices are not axisymmetric, but become symmetric about 5 diameters downstream of the body. They found the vortex velocity distributions at downstream distances of 5 to 16 diameters to be those of convected Oseen vortices. The optical interferometer method was also used to measure the surface deformation in the wakes of a cylinder. From the very small distortion of the free surface, they calculated the strength and age of the vortices as function of the distance from the cylinder.

Mathelin et al. [17, 18] employed a heated subsonic wind tunnel to experimentally investigate the dynamical and thermal behaviors of the flow around a circular cylinder submitted to blowing. In [17], they selected the injection rate and main flow temperature to be the experimental parameters for Reynolds numbers from 3,900 to 14,000. They reported that the velocity and temperature profiles are modified similarly with the blowing, as the injection thickens the boundary layers and changes their shapes. For the case that the Reynolds number is 3,900 and the temperature of injected and main flow remains at 20°C, the

dynamical boundary layer thickness is reported as a function of the injection rate for an angle of 70° , measured from the front stagnation point. The thicknesses are $0.04D$, $0.05D$, and $0.08D$ for the injection rates are 0%, 2%, and 5%, respectively. The blowing in this investigation is proved to strongly affect the boundary layer, including thickness and stability, and to considerably promote their separation. Besides, in [18], the strong impact of the blowing on the dynamics was also illustrated by measuring some static pressure profiles in the near wake. They found that the wake is proved to widen with blowing. It is quite like a phenomenon that the apparent cylinder diameter becomes larger. Furthermore, due to the net injection mass into the flow, the defect of wake static pressure decreases with the blowing. They also emphasized the blowing impact on the Strouhal number to study the modification of the stability patterns. The effect of Strouhal number was investigated by varying the blowing conditions. It exhibited a linearly decrease of the vortex shedding frequency with the blowing ratio until a saturation state was reached. The main flow temperature influence was also investigated and it was shown to have no effect on the Strouhal number evolution. Besides, a relation to predict the equivalent Reynolds number (Re_{eq}), which corresponds to a flow without injection but with the same value of Strouhal number, was derived. That is,

$$Re_{eq} = 300 - 250(1 - e^{-F/2}).$$

The relation makes easily to account the blowing, giving the characteristics of the flow subjected to injection and the expected Strouhal number, which is correlated to the modified Reynolds numbers.

Almost ten years ago, three-dimensional phenomena and aspects have been the subjects for many experimental and numerical studies. Zhang et al. [19] investigated the transition of the cylinder wake by experimental study in a water channel and by numerical simulation using a finite-difference scheme, respectively. They observed four different physically instabilities, namely, a local vortex-adhesion mode, and three near-wake instabilities, which are A-, B-, C-mode. Any of these four instability processes can arise in a confined range of Reynolds numbers from 160 to 230. The vortex-adhesion is easily to be distinguished from the other modes since it represents a local deformation of the primary von Kármán vortices. Yet other instabilities are associated with global, secondary vortices on the von Kármán vortices. They compared the three secondary vortices with each other and reported that the three modes are associated with different spanwise wavelengths of roughly 4, 1, and 2 diameters of the cylinder, respectively. They also found four different kinds of transition scenarios from both experiment and simulation. They are a hard vortex-adhesion, a soft A-mode, a controlled C-mode, and a retarded transition. In which, the irregular vortex-adhesion mode and the time-periodic A mode can be regarded as stable coexisting roughly in the range $170 < Re < 230$. The soft C-mode transition can be observed by numerical and experimental investigations with a thin wire, located in the near wake. Finally, the retarded transition is the direct transition from 2-D shedding to B-mode at $Re \sim 230$. Similarly, Brede et al. [20] used particle image velocimetry (PIV) to investigate the transition of the circular cylinder wake. The range of Reynolds numbers they selected is from 160 to 500. They found that the instantaneous circulation

of the streamwise vortices is different, namely, two classes of secondary vortices, A- and B-mode. The two modes represent different types of vortex structures with different topologies. The spanwise wavelengths of the two modes are the same as those mentioned previously. They indicated that the instability of the braid region between the primary Kármán vortices due to centrifugal forces results in the A-mode. Besides, the B-mode is likely to originate from the instability of the separating shear layer in the near wake. They also concluded that the A- and B-mode structures of the Kármán vortex street are common features of the 3-D transition of free shear flows. The initial appearance of the three-dimensional instability in the separated region over the circular cylinder was visualized and reported by Yokoi and Kamemoto [21]. They selected the range of Reynolds numbers from 230 to 1,340 and carried out the experiment in a towing water tank. They found that the three-dimensional features of boundary layer separation are represented by the recirculating flow in the separated region. Moreover, they confirmed that the spanwise distance l_z divided by the diameter of the cylinder reduces as the increase of the Reynolds numbers ranged from 230 to 1,340. (l_z is the spanwise distance between adjacent spread spots or upstream singular separation points.)

Flow visualization through the use of the smoke-wire technique was carried out by several researches. Fukamachi et al. [22] suggested the improvement for the smoke-wire technique. They mentioned that one of the serious drawbacks of the method, which is a simple but very useful means of flow visualization in low-speed wind tunnel studies, is the short

existing duration of the smoke. In their study, they showed that the duration time can be greatly increased by mixing a fine metal powder with the oil. Another paper, which mentions the developments in smoke flow visualization, was presented by Mueller [23]. He described the developments in the generation, the injection of smoke as well as the lighting and data processing. The developments showed clearly that although the smoke visualization is one of the oldest flow visualization techniques in wind tunnels, it still continues as an important experimental tool in the study of complex fluid dynamic phenomena.

1.3 Scope of Present Study

The cold flow field visualization carried out in the study consists of two parts, as shown in Fig. 1.3. The first one is to visualize the flow field around and behind the burner without fuel blowing. The experimental results are used to compare with the ones observed by previous researchers. The purpose is to confirm the experimental credibility in the present study. In the second part, the air is used and ejected from the burner into the incoming air flow. The porous burners used in this study have two types. One is cylindrical type modified from the original design of Chang [2] but without cooling groove. The other type is spherical one. The aim of the present investigation is to visualize the cold flow fields over the burners with blowing throughout the whole surface. The parameters are incoming flow velocity, blowing ejection velocity and geometric variations of burner. The results of the flow visualization are described in detail. The resultant photographs will be introduced to

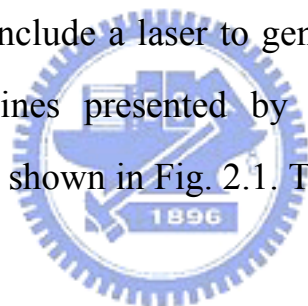
comprehend the flame behaviors over for the cylindrical burners by the influence of flow structures. In particular, the physical mechanisms of the lift-off flame and the second wake flame are identified more clearly. Finally, the flow patterns taken by a digital video are used to measure the separation angle that originated from the front stagnation point to the separation one. The purpose is to investigate the relationship between the separation angle and the Reynolds number.



CHAPTER 2

EXPERIMENTAL APPARATUS

The experimental apparatuses in the present study basically are the same as those of Chang's equipments [2], except the applications of the smoke-generation wire and the laser-sheet lighting, which are used to visualize the cold flow field around and behind the cylinder or sphere burner. The smoke-generation technique is described in detail by the textbook [24]. The apparatus consists of three major elements, which are the wind tunnel, the porous sintered burner and the measurement instrumentations, which include a laser to generate an illuminating sheet to visualize the streamlines presented by the smoke particles. The structural configuration is shown in Fig. 2.1. The detailed descriptions are given as follows.



2.1 Wind Tunnel

A wind tunnel is designed to be able to provide a laminar, uniform oxidizer flow to the porous burner. It is open-circuit and oriented vertically upwards. The tunnel comprises five parts, which are the blower, diffuser, flow straightener, contraction and test section. The design concepts about the wind tunnel are mainly from a NIST paper [25], and also comply with the standard of AMCA210-85 [26]. The schematic configurations are shown in Fig. 2.2 and Fig. 2.3.

2.1.1 Blower

A variable-frequency blower supplies the airflow in the tunnel. The frequency is directly converted into desired velocity by a converter. Chen [27] employed the hot wire to measure the velocities to obtain the correlation between the blower frequency and resultant velocity in test section demonstrated in Fig. 2.4. In order to avoid the influence of vibration, the bases of wind tunnel and blower are separated by a flexible plastic ductwork, as shown in Fig. 2.5.

2.1.2 Diffuser

A diffuser long 30-cm has an inlet cross-section area of $12 \times 12 \text{ cm}^2$ and the outlet one is $40 \times 40 \text{ cm}^2$. The expansion ratio based on area is 1:11.



2.1.3 Flow Straightener

Before entering the contraction section, the airflow from diffuser section is unstable. The flow straightener, consisting of honeycomb and screen, is designed to ensure that the inflow is laminar and uniform.

2.1.4 Contraction Section

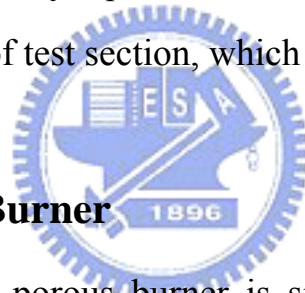
The purpose of contraction section is to provide a uniform flow field into the test section. The design standards need to shorten the duct and reduce boundary layer thickness along the wall as possible.

2.1.5 Test Section

The test section has a cross section area of $24 \times 4 \text{ cm}^2$ and a length of 35 cm. It is composed of four sides. In the front and two adjacent sides,

they are equipped with quartz-glass plates served as the observation windows. The laser sheet is allowed across the test section from one of the side quartz-glass plates to another. The rear side is made of a stainless steel plate for supporting the inserted burner. The downstream of test section is connected with a diffuser, used to reduce the velocity of exhaust gases from test section. A vent follows after the diffuser to outdoor. At the rim of test-section entrance, there exist seven holes as shown in Fig. 2.6 to let sensors insert into flow field for confirming its uniformity. The sensors are hot wires as mentioned previously. They are used to confirm the uniformity and stability of the flow if the measured values by hot wires are nearly equal. Moreover, a smoke-generation wire is set up in the upstream of test section, which will be described later.

2.2 Porous Sintered Burner



The material of the porous burner is sintered stainless steel. The burners used in this thesis have two types. One is cylindrical type and the other is sphere one. Each type of burner has two different designs. The detailed descriptions are given as follows.

2.2.1 Cylindrical Burner Structure

The structures of cylindrical burner (see Fig. 2.7) are modified from the original design of Chang [2]. The burners consist of the inner and outer parts. In the outer part, each of them is a replaceable porous cylinder, which is 20 μ m pores and has a length of 40 mm. The inner and the outer diameters for one of the cylinders are 14 mm and 20 mm,

respectively (see Fig. 2.8). Nevertheless, the inner and the outer diameters for the other one are 9 mm and 15 mm, respectively (see Fig. 2.9). In the inner part, the burner is a cylindrical brass rod (see Fig. 2.10) with fuel supply groove. In the present experiment, the air is used to be the fuel. The outer part is screwed onto the inner part. The advantage of this design is that the burner replacement can be easily performed.

2.2.2 Spherical Burner Structure

The design of the sphere is based on several important criteria. The burner has to be robust, easily built, installed, and operated, and able to generate reliable screen test data. The outer diameter of the sphere is 15 mm. The porous sphere is dug a fillister in order to connect to the gas transport line. The diameter and the depth of the fillister are 6.35 mm and 9.8 mm, respectively (see Fig. 2.11). Because the air needs to supply into the sphere, therefore, two kinds of transport line designs are considered. They are shown as Fig. 2.12 and Fig. 2.13. One is in vertical orientation parallel to the flow direction in wind tunnel, the other is in horizontal orientation across the stream. Both designs are expected to affect the flow field.

2.2.3 Burner Equipped to Test Section

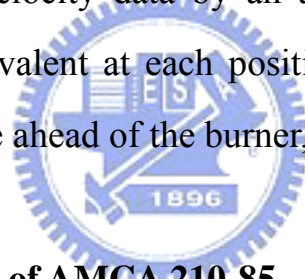
In the present experiment, the air is used to supply into the burner. The flow rate of air is controlled and measured by a digital flow meter (for air). There is a digital mass flow controller dominated by a high capability of microprocessor inside the flow meter. A 16-bit A/D converter in the CPU digitizes the flow rate and control signal, and then

transforms them into analog ones. The air ejection velocity is computed by dividing the air volumetric flow by the available air ejection area along burner surface.

2.3 Measurement Instrumentations

2.3.1 Hot Wire for IFA 100 Diagnostics

The objective using hot wire (Fig. 2.14) for IFA 100 Diagnostics (Fig. 2.15) is to confirm flow uniformity in the test section of wind tunnel. It generates a bridge voltage when hot wire is inserted into the holes of test section. The original data of voltage obtained from hot wire is converted into desired velocity data by an acquisition program. If the velocities are rather equivalent at each position, it can be sure that the flow is uniform and stable ahead of the burner, as shown in Fig. 2.16.



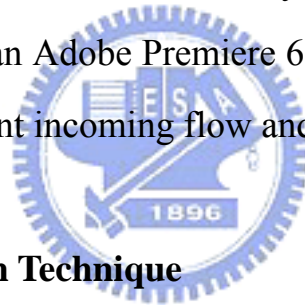
2.3.2 Nozzle of Standard of AMCA 210-85

The measurement of inflow velocity at the test section adopts the AMCA 210-85 standard of nozzle-method to measure the volume flow rate and then to deduce the flow velocity. The standard is used to establish uniform flows for laboratory testing of fans and other air moving devices by AMCA. There are three nozzles (Φ : 10, 15, and 30 mm) and four sets of pitot tubes distributed uniformly inside the cylinder as shown in Fig. 2.3. They are used to measure the local velocities inside the cylinder. Then it can get total volume flow rate to deduce velocity of test section by dividing cross section area of test section. The accuracy, described by AMCA 210-85, is within 3% when velocities are ranged

from 0.21 m/sec to 3.3 m/sec, but it becomes 5% as the velocity is smaller than 0.21 m/sec.

2.3.3 Digital Video

A digital video (Type DCR-TRV40, SONY) is used to visualize the flow field. It is fixed at an appropriate position to record flow field variations. In order to catch the phenomena in the dark environment, it is necessary to process images digitally to obtain special effect. In the present experiment, the function (B & W) of the picture effect is used to make the picture appears in monochrome (black-and-white). The images from the video are transmitted to a PC by IEEE 1394 card, and the images are processed by an Adobe Premiere 6.0 software to show a series of flow patterns in different incoming flow and air ejection velocities.



2.3.4 Smoke-Generation Technique

The smoke-generation technique has been developed to measure velocity profiles in boundary layers at the very early beginning. It also has been used well to visualize the complex three-dimensional flows; for instances, the separation bubbles, the flow structures in turbulent free shear flows and boundary layers, a jet in a cross-flow and the Kármán vortex street behind a circular cylinder. In the present study, the technique for flow visualization in low speed wind tunnels is utilized to investigate the cold flow behaviors past a cylindrical or a spherical burner. The schematic configuration is shown in Fig. 2.17. It consists of two major parts, which are the fine metal wire, and the oil to produce smoke. Both of them are described in the following.

2.3.4a Metal Wire

The fine wire is heated to vapor the oil by means of an electric current. Once the oil is vaped, the smoke-wire is generated. For experimental requirement, many metals with sufficient strength and electrical resistance can be used, but the commonly used ones are made of stainless, nichrome and tungsten. Moreover, the size of the wire is not arbitrarily selected, and it is dictated to some extent by the flow speed in test section. At lower flow speeds, it is better to use a smaller diameter wire that produces smoke sharply. For higher speed flow applications, it is recommended to use a larger diameter wire because the larger wire surface area can maintain a higher smoking rate. The wires are typically stretched so taut that the larger ones can be able to accommodate the required tension at a higher temperature. Reynolds number is another factor that must be considered when deciding the wire size. In order to minimize the flow disturbance, the Reynolds number based on the wire diameter should not be larger than 20. According to the above-mentioned, the diameter of wire is selected as 0.1mm and the wire is made of stainless in the present study.

2.3.4b Oil

There are various kinds of oil which can be used to produce smoke filaments, including lubricating oil, silicon oil, model train oil, paraffin and kerosene. In the present experiment, a solution of organic oil in water is adopted. The advantages of the solution are that it is nontoxic, nonflammable and non-explosive. Besides, it is simple to clean up. However, there is a light alcohol smell produced after vaporizing the

solution.

It is necessary that the wire be coated uniformly with the oil to make certain that the smoke is produced evenly along the length of the wire. A special design to coat the oil onto the wire is employed in the experiment. The foamy-cotton with oil is brushed through the wire by pulling the manual movement mechanism. The structural configuration is shown in Fig. 2.18.

2.3.5 Laser-Sheet Lighting

The laser sheet is used to visualize the flow features. A thin sheet of light can be generated easily by using a cylindrical lens and a light source, like a laser. The power of the laser used is 50 mw, and it generates green light. The spreading angle of the sheet depends on the diameter of the lens: the smaller the diameter, the larger the spreading angle. Once the laser sheet is formed, it is ready to be used for “sectioning” the flow field, usually by aligning the plane of the light sheet perpendicular to the line of view. Moreover, the set-up position of laser is on the side of test section to visualize the smoke flow from the obverse side, and the height is changed arbitrarily from the upstream of the test section (see Fig. 2.19). The experimental system is located in a darkroom to improve the contrast of the flow photos.

2.4 Procedure of the Experimental Operation

- (1) Calibrate the instruments to insure the stabilization and accuracy of their performance before performing the experiment.
- (2) Warm up the apparatuses, such as blower and mass flow

controller.

- (3) The blower has to be operated for 30 minutes in advance until the flow uniformity and stabilization are achieved.
- (4) Check if any fuel gases leakage from pipelines by applying suds on them. It is necessary to make sure the accuracy of the fuel (air) flow rate and ejection velocity.
- (5) Open the valve of air fuel cylinder and retain the inlet pressure up to 0.55 kg/cm^3 , then turn on the stop valve of mass flow controller. When the alarm light of mass flow controller displays green, it indicates that the fuel passes pipelines to burner.
- (6) Turn on laser sheet and shine on the appropriate position to visualize the flow field.
- (7) Set the fuel flow rate to the desired value. At first a certain fixed value of fuel supply is chosen to the burner, and then increase the inflow velocity slowly to get various flow visualizations over the burner.
- (8) Set the digital video in fixed position to get the same observation view of test section to catch all images from the flow field.
- (9) Also change the fuel ejection rate as a parameter under a fixed flow velocity. Carry out the similar procedure as the above.
- (10) Change the different burner to repeat the above-mentioned procedure and investigate the difference of the results.

CHAPTER 3

UNCERTAINTY ANALYSIS

The accuracy of the data from experimental results should be confirmed before the analyses of experimental results are carried out since the data may not be equally good to adopt. Uncertainty analysis (or error analysis) is a procedure used to quantify data validity and accuracy [28]. Experimental measuring results in errors. Experimental errors can be classified into the fixed (systematic) error and random (non-repeatability) error, respectively [28]. And fixed error is the same for each reading and can be removed by proper calibration and correction. Oppositely, random one is different for every reading and hence cannot be removed. The purpose of uncertainty analysis is to estimate the probable random error in experimental results.

From the viewpoint of reliable estimation, it can be categorized into single-sample and multi-sample experiments. If experiments could be repeated enough times by enough observers and diverse instruments, then the reliability of the results could be assured by the use of statistics [29]. Like such, repetitive experiments would be called multi-sample ones. Experiments of the type, in which uncertainties are not found by repetition because of time and costs, would be called single-sample experiments.

3.1 Analyses of the Propagation of Uncertainty in Calculations

Uncertainty analysis is carried out here to estimate the uncertainty

levels in the experiment. Formulas for evaluating the uncertainty levels in the experiment can be found in many papers [29, 30] and textbooks [28]. They are presented as follows:

Suppose that there are n independent variables, x_1, x_2, \dots, x_n , of experimental measurements, and the relative uncertainty of each independently measured quantity is estimated as u_i . The measurements are used to calculate some experimental result, R , which is a function of independent variables, x_1, x_2, \dots, x_n ; $R = R(x_1, x_2, \dots, x_n)$.

An individual x_i , which affects error of R , can be estimated by the deviation of a function. A variation, δx_i , in x_i would cause R to vary according to

$$\delta R_i = \frac{\partial R}{\partial x_i} \delta x_i. \quad (3-1)$$

Normalize above equation by dividing R to obtain

$$\frac{\delta R_i}{R} = \frac{1}{R} \frac{\partial R}{\partial x_i} \delta x_i = \frac{x_i}{R} \frac{\partial R}{\partial x_i} \frac{\delta x_i}{x_i} \quad (3-2)$$

Eq. (3-2) can be used to estimate the uncertainty interval in the result due to the variation in x_i . Substitute the uncertainty interval for x_i ,

$$u_{R_i} = \frac{x_i}{R} \frac{\partial R}{\partial x_i} u_{x_i} \quad (3-3)$$

To estimate the uncertainty in R due to the combined effects of uncertainty intervals in all the x_i 's, it can be shown that the best representation for the uncertainty interval of the result is [30]

$$u_R = \pm \left[\left(\frac{x_1}{R} \frac{\partial R}{\partial x_1} u_1 \right)^2 + \left(\frac{x_2}{R} \frac{\partial R}{\partial x_2} u_2 \right)^2 + \dots + \left(\frac{x_n}{R} \frac{\partial R}{\partial x_n} u_n \right)^2 \right]^{1/2} \quad (3-4)$$

3.2 Uncertainty Level Analysis in the Experiment

The results of all uncertainty analysis according the calculations of above formula are summarized in Table 3.1. Several parameters are selected to demonstrate the process of uncertainty level analyses as follows:

(1) The cross-section area of test section, A ,

$$A = a \times b, \quad a = 240 \pm 0.5\text{mm}, \quad b = 40 \pm 0.5\text{mm}$$

$$A = A(a, b)$$

$$u_a = \frac{0.5}{240} = 0.00208, \quad u_b = \frac{0.5}{40} = 0.0125$$

$$u_A = \pm \left[\left(\frac{a}{A} \frac{\partial A}{\partial a} u_a \right)^2 + \left(\frac{b}{A} \frac{\partial A}{\partial b} u_b \right)^2 \right]^{1/2} = \pm \left[(u_a)^2 + (u_b)^2 \right]^{1/2} = \pm 0.01267$$

(2) The surface area of sphere burner, $A_{s,B}$,

$$A_{s,B} = \pi D^2, \quad D = 15 \pm 0.5\text{mm}$$

$$A_{s,B} = A_{s,B}(D)$$

$$u_D = \frac{0.5}{15} = 0.03334$$

$$u_{A_B} = \pm \left[\left(\frac{D}{A_B} \frac{\partial A_B}{\partial D} u_D \right)^2 \right]^{1/2}$$

(3) The surface area of cylinder burner, $A_{c,B}$,

$$A_{c,B} = \pi D L_B, \quad D_1 = 20 \pm 0.5\text{mm}, \quad D_2 = 15 \pm 0.5\text{mm}, \quad L = 40 \pm 0.5\text{mm}$$

$$A_{c,B} = A_{c,B}(D, L)$$

$$u_{D_1} = \frac{0.5}{20} = 0.025, \quad u_{D_2} = \frac{0.5}{15} = 0.03334,$$

$$u_L = \frac{0.5}{40} = 0.0125$$

$$u_{A_{c,B}} = \pm \left[\left(\frac{D}{A_{c,B}} \frac{\partial A_{c,B}}{\partial D} u_D \right)^2 + \left(\frac{L}{A_{c,B}} \frac{\partial A_{c,B}}{\partial L} u_L \right)^2 \right]^{1/2}$$

(4) The uncertainty of inflow velocity

$$U_{in} = \frac{\dot{V}_0}{A}, \quad U_{in} : \text{Incoming flow velocity}, \quad \dot{V}_0 : \text{Flux of air}$$

$$u_{U_{in}} = \pm \left[(u_{\dot{V}_0})^2 + (-u_A)^2 \right]^{1/2}$$

(5) The uncertainty of fuel-ejection velocity

$$V_w = \frac{\dot{V}_0}{A_{Burner}}, \quad V_w : \text{Fuel (air) velocity}, \quad \dot{V}_0 : \text{Flux of fuel (air)}$$

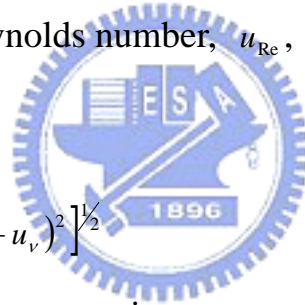
$$V_w = V_w(\dot{V}_0, A_{Burner})$$

$$u_{V_w} = \pm \left[(u_{\dot{V}_0})^2 + (-u_{A_{Burner}})^2 \right]^{1/2}$$

(6) The uncertainty of Reynolds number, u_{Re} ,

$$Re = \frac{U_{in} D}{\nu}$$

$$u_{Re} = \pm \left[(u_{U_{in}})^2 + (u_D)^2 + (-u_\nu)^2 \right]^{1/2}$$



(7) The uncertainties of the properties,

$$u_{\rho(T)} = \pm \frac{\delta \rho}{\rho} = \frac{1}{\rho} \frac{d\rho}{dT} (\pm \delta T)$$

$$u_{\nu(T)} = \pm \frac{\delta \nu}{\nu} = \frac{1}{\nu} \frac{d\nu}{dT} (\pm \delta T)$$

3.3 The Experimental Repeatability

In order to confirm the accuracy and coincidence of the experiment, each case under a specific inflow velocity over a 15mm-diameter cylinder burner without blowing to measure the separation angle between the front stagnation and separation points was executed three times to ensure the repeatability. Fig. 3.1 shows the measured angles as a function of Re

number. For each incoming flow velocity, three measured data are recorded and the corresponding average value, indicated by a dashed curve, is given as well. The three measured data, their averaged value and the related error are listed in Table 3.2. The error is defined as the ratio of the absolute difference value between the maximum and minimum ones among the three measurements to their averaged value. It can be seen that the maximum error is less than 10%, apparently, they are within the acceptable range. We can conclude that the repeatability is quite good. Fig. 3.2 shows the presentation graphically of Table 3.2. The procedures for measuring the separation angles between the front stagnation and separation points will be described in next chapter. Moreover, their corresponding phenomenal analyses will be discussed in detail.



CHAPTER 4

RESULTS AND DISCUSSION

The main subject of the present experiments is to investigate the flow patterns around a cylindrical or spherical burner, which was submitted to blowing. The experimental parameters adopted in the thesis are the variations of the incoming flow velocity (U_{in}) and the air ejection velocity (V_w) for two types of burners. Each type of burner has two different designs. For the cylindrical burner, two different diameters of burner, which are 15mm and 20mm, respectively, are used. On the other hands, two kinds of fuel transport line designs for the spherical one are considered. One is in vertical orientation parallel to the main flow and the other is horizontal orientation. However, the interference with the flow in the former design is so intense that the flow pattern around the burner can not be observed explicitly. The corresponding photograph is shown in Fig. 4.1. Thus, only the flow around the horizontal design of the sphere is considered in the following sections. The range of the incoming flow velocity is from 0.15 m/s to 2.29 m/s. The air ejection velocity ranges from 1.41 cm/s to 2.64 cm/s for the 15mm-diameter cylindrical burner, whereas it is from 1.06 cm/s to 1.98 cm/s for the 20mm-diameter cylindrical one. As to the sphere burner, it is ranged from 1.18 cm/s to 7.08 cm/s. However, the flow visualizations for the flow patterns around the cylinders and the spheres without blowing are carried out first in the thesis. The purpose is to confirm the correctness of the experimental results in advance. The descriptions are given in detail as follows.

4.1 Flows Around and Behind the Burner without Blowing

4.1.1 Flow Behaviors for Cylindrical Burners

For the case of the flows around the cylindrical burners, two series of photographs are shown in Fig. 4.2 and Fig. 4.3, respectively. Fig. 4.2 presents the flow patterns associated with 15mm-diameter cylinder, whereas Fig. 4.3 shows the corresponding ones with 20mm-diameter cylinder. The varying parameter for both cases is the incoming flow velocity. The Reynolds numbers, $Re = \frac{U_{in} D}{\nu}$, where ν is the kinematic viscosity of incoming air (300K, 1atm) and is equal to $1.57 \times 10^{-5} \text{ m}^2/\text{s}$, are ranged from 143 to 2,092 for the 15mm-diameter cylinder and those are from 191 to 2,356 for the 20mm-diameter one.

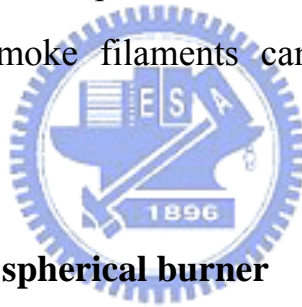
In Fig. 4.2(a), where Re is 143, the vortices behind the cylinder are observed. At the very beginning of smoke generation, the smoke filaments springing from the separation points of the cylinder are oscillatory. It persists for a few seconds until the downstream smoke rolls back toward the rear of cylinder. After that, two vortices in different size present. The bigger one occupies almost the whole wake behind the cylinder and the smaller one is observed only in the left or right of the far wake. The above observed phenomena cannot be clearly demonstrated in a single picture. However, it can be seen in the video type, which is not included in this thesis. Most important, such manner of formation and development of the vortices can be confirmed by Nayler and Frazer [14] as illustrated in Fig. 4.4. They conducted experiments at a Reynolds number about 120. At first, the lower vortex is formed by the fluids that are from the upper side of the cylinder, as shown in Fig. 4.4(a)-(d). After

that, a great deal of fluids from one side of the wake flow between the vortices and approach the other side of the wake; see Fig. 4.4(f)-(h).

Fig. 4.2(b) is taken at $Re = 210$, where smoke filaments show the periodic shedding of vortices. The two different sizes of vortices mentioned previously in Fig. 4.2(a) are also observed, but they become more or less the similar size. However, they are hard to visualize very clearly because of the increase of the incoming flow velocity, which lead the majority of smoke to the downstream and only the minority of smoke are recirculated back to the rear of the cylinder. The similar pattern is observed by increasing the Re to 372, shown in Fig. 4.2(c). The kármán vortex street is clearer to visualize. Two vortices occupy the wake behind the cylinder alternately. It can be seen that the pattern seems to be disintegrated at the downstream of the wake. However, the case of Re equal to 372 is near the upper limit for stability by visualization.

In Fig. 4.2(d), where Re is 544, the disintegrations of flow pattern at the downstream of the wake occur earlier than that mentioned previously. And the vortices in the wake are vague to identify. They mix up together and change into turbulence. Until Re is up to 2,092, the flow pattern appears a different type from the previous one. As shown from Figs. 4.2(e) to (h), the kármán vortex street becomes invisible by increasing Re as mentioned previously. For $Re = 2,092$, it is laminar over the front of the cylinder, separates, and breaks up into a turbulent wake. Moreover, the flow pattern vibrates on both sides. The flow patterns shown in Fig. 4.2(b) ($Re = 210$) and Fig. 4.2 (h) ($Re = 2,092$) are quite similar to those in Figs. 4.5 and 4.6, respectively, obtained by Koopmann ($Re = 200$) and Wérle and Gallon ($Re = 2,000$) in an album of fluid motion [31].

Even though the diameters of the cylinders in Fig. 4.2 and Fig. 4.3 are different, the flow patterns for both cases are similar to each other. However, for the 20mm-diameter cylinder, the critical Re , above which the wake breaks up into a turbulent one, is lower than the corresponding Re for 15mm-diameter cylinder. Fig. 4.3(c) shows the flow pattern at the Re is 496, in which the vortex street is indistinct, and the wake behind the cylinder is turbulent. It is due to the rough surface area of the 20mm-diameter cylinder is greater than the one of the 15mm-diameter cylinder. The rough surface hastens the wake to become turbulent. Furthermore, Fig. 4.7 shows a series of schematic illustrations plotted by using free hand. They are correspondent to those pictures in Fig. 4.3. The flowing trends of the smoke filaments can be seen clearly via the diagrams.



4.1.2 Flow behaviors for spherical burner

Unlike two-dimensional flows, such as the flow over a cylinder, the flow over a sphere is considered as a three-dimensional flow, which is more complicated. The sequence of photos shown in Fig. 4.8 are the flow patterns associated with the flow past a porous sphere and the corresponding range of Re is from 143 to 2,092, where Re is based on the sphere diameter and the incoming flow velocity U_{in} , and the kinematic viscosity ν of incoming air is the same as the one for the case of cylinder mentioned previously.

Fig. 4.8(a) shows the flow pattern at $Re = 143$, the wake behind the sphere is steady and axisymmetric. The vortex-ring is observed in the rear of the sphere. The length of the vortex-ring is approximately the sphere

diameter. The front part of vortex-ring is stably attached to the sphere. However, the oscillation is found to exist at the rear of the vortex-ring. The diagrammatic illustration shown in Fig. 4.9 is used to illustrate the flow pattern mentioned above. According to the previous research conducted by Taneda [6], he found that when Re is about 130, the rear of vortex-ring in the wake behind the sphere begins to oscillate with a very long period. He also measured the size of the vortex-ring. The observed phenomena in the present work are similar the findings of Taneda [6].

Fig. 4.8(b) is the flow pattern at $Re = 210$. The wake behind the sphere is still steady but becomes non-axisymmetric since the vortex-ring shifts away from the axis. Moreover, the smokes from the wake form two parallel threads. The size of vortex-ring is bigger than the one in Fig. 4.8(a). Its length is about 1.4 times of the sphere diameter. A similar wake form is obtained as well in Fig. 4.8(c), as Re is 372. Nevertheless, the two threads become nonparallel. The vortex-ring grows and the length is about 1.8 times of the sphere diameter. It becomes more and more elongated. With these three measurements, it is found that the size of the vortex-ring is a linear function of $\log Re$, which is found by Taneda [6].

The onset of the unsteady wake is found at $Re = 458$ (see Fig. 4.8(d)). The double-thread wake becomes unstable and finally the vortex begins shedding from the rear of sphere. The vortex-ring mentioned above is observed in the wake but it is hard to measure the length of the ring vortex due to the appearance of very slight smoke. The two threads separate and merge alternately along the axis of the sphere. As the Re increases further, $Re = 621 \sim 2,092$, the resultant patterns shown in Fig. 4.8(e)-(h) are similar to the one in Fig. 4.8(d). At this range of Re , the

wake behind the sphere becomes more chaotic.

4.1.3 Position of separation

The separation angle, measured from the front stagnation point to the separation one, is determined by examining the photos for the cylindrical and spherical burners. Fig. 4.10 illustrates the measurement procedure. The results are presented in Fig. 4.11 and Table 4.1-4.2, respectively.

For the case of the sphere ($D = 15\text{mm}$), the separation angles are ranged from 105° to 123° . The maximum angle, 123° , is correspondent to $Re = 143$, whereas the minimal one, 105° is to $Re = 1,768$. In the range of Re from 143 to 793, the angle reduces slightly with an increase of Re . However, a sharp increase of separation angle is observed at $Re = 870$. Behind that, the descendent tendency of the angle with increasing Re appears, even though there are some slight oscillations observed in the range. It is confirmed that the separation points move forward to the front part of sphere as the Re is increased.

For the case of cylinder, the instable oscillation is more apparent than that of the sphere. The separation angles are ranged from 95° to 111° for the 15mm-diameter cylinder and that from 93° to 116° for the 20mm-diameter one.

With the same diameter, the separation occurrence for the cylinder is earlier than that for the sphere one because the flow is subjected more frictional force in cylinder case. Moreover, the variation of angle with an increase of Re for the bigger cylinder is more intense than the small one. It may be attributed to the rough surface area which can arise the different

levels of turbulence. The descendent tendency of the angle with the increasing Re is nonexistent in cylinder case.

4.2 Flows Around and Behind the Burner with Blowing

The section is the emphasis in this thesis. In order to clarify the effects upon the flow of burner with blowing, several experiments are carried out. Under the various air ejection velocities (V_w), the resultant flow patterns associated with varying Re are visualized. The flow pattern for each burner with a fixed (V_w) is described in detail as follows.

4.2.1 Flow Behaviors for Cylindrical Burners

For the case of 15mm-diameter cylinder, V_w is set at 1.76 cm/s to eject throughout the whole cylinder surface. A series of photos shown in Fig. 4.12 presents the variations of flow patterns with increasing Re . In Fig. 4.12(a), $Re = 143$, the wake observed is different from the one in Fig. 4.2(a). The separation points are blown off a distance from the cylinder surface. It looks like the flow around a bigger cylinder relative to the original one without blowing. The smoke filaments springing from the separation points oscillate slightly. Eventually, a few of smokes in downstream are drawn into the wake, which does not connect with the rear of the cylinder. However, the vortices are almost separated into both sides of wake because of the effect of the blowing. As Re increases to 210 (Fig. 4.12(b)), the periodic vortex shedding shows up. The wake is observed to get closer to the rear of cylinder. The separation points are still blown off from the surface of cylinder, but the distance they stand is

shorter than that in Fig. 4.12(a). The vortices formation in the wake is changed, too. The vortices mentioned in Fig. 4.12(a) now begin to intermix as shown in Fig. 4.12(b), which is due to the greater strength of vortices to resist the ejection effect. After that, as Re of 372 is approaching (see Fig. 4.12(c)), the appearance of vortex street becomes obvious. The vortices in the wake form a similar pattern to the one that the cylinder without blowing, mentioned previously. However, it appears more chaotic. The distance between the wake and rear surface of cylinder becomes smaller. It is concluded that the wake is getting more and more closer to the rear surface of cylinder as Re increases, as illustrated from Figs. 4.12(a) to (d). The wake does not approach to the cylinder surface until Re is 907 (Fig. 4.12(e)). The wake returns to the rear of cylinder and it looks like that there is no ejection from the cylinder. It may be attributed to the pressure distribution of the flow field. Once the static pressure of the downstream wake is greater than the one caused by the blowing over the cylinder surface, the wake is pressed back to the rear of cylinder. After that, the blow-off wake is no longer obtained as Re is increased; see Fig. 4.12(e)-(f).

V_w of 1.32 cm/s is selected for the 20mm-diameter cylinder. Fig. 4.13 presents the similar flow behaviors as those in Fig. 4.12. In Fig. 4.13(a), as Re is 191, the flow pattern for the cylinder with blowing is observed. The separation points are not on the cylinder surface because of the blowing. The smoke filaments originating from the separation points oscillate intensely. The downstream smokes are drawn into the wake and form the irregular vortices in the wake. The vortices circulate toward to the rear of cylinder and finally become almost horizontal at the front part

of wake. The wake stands a distance from the rear surface of cylinder. As Re is increased to 280 (see Fig. 4.13(b)), the vortex shedding is observed. The interval between the wake and the rear of cylinder reduces. There are two apparent vortices alternating with each other at the downstream of wake. However, they become chaotic as soon as they approach to the border between the wake and the cylinder. It is due to the interference of blowing with the wake. Fig. 4.13(c), $Re = 496$, shows that the appearance of vortex street is more evident. The wake gets closer to the rear of cylinder. The vortices in the wake are turbulent. As Re is increased to 611 even to 726 (Fig. 4.13(d)), the pattern is disintegrated at the downstream wake. The vortex street seems to be irregular. However, the wake does not attach to the rear of cylinder until Re is 1,057, as shown in Fig. 4.13(e). The pattern is similar to the one in Fig. 4.3(f), whose cylinder is without blowing. The reason is the same as that mentioned previously. Comparing photos in Fig. 4.13 with those in Fig. 4.3, it can be seen that the onset of Re , above which vortex street is observed, in the former case (with blowing) is greater than the one in the latter. The onset of Re in Fig. 4.13 is 280, whereas corresponding Re is no more than 191 in Fig. 4.3.

4.2.2 Flow Behaviors for Spherical Burner

Regard to the case of sphere, V_w of 4.72 cm/s is selected. Fig. 4.14 shows the flow behaviors as a function of Re . In Fig. 4.14(a), Re is 143 and the wake behind the sphere is shown. At the beginning of smoke generation, the smoke filaments spring from the separation points, which are blown off a height from the sphere surface. After that, the downstream smokes are drawn into the wake and form the axisymmetric vortex-ring.

However, unlike the vortex-ring mentioned in section 4.1.2, the front part of vortex-ring is not attached to the rear of sphere. Due to the effect of the blowing, the axisymmetric vortex-ring is separated and shown an “ Λ ” shape. It also can be observed that the rear part of vortex-ring oscillates slightly. As Re reaches 210 (Fig. 4.14(b)), the wake is still axisymmetric. The front parts of vortex-ring are closer to the rear of surface but are not attached either. The “ Λ ” shape vortex-ring is not obtained and the vortex-ring seems not to be affected by the blowing. Two threads are formed with smokes from the wake and they begin shedding. The non-axisymmetric wake is observed in Fig. 4.14(c), which Re is 372. The vortex-ring shifts off the axis. The wake is still not connected with the rear of surface. The similar pattern is also observed in Fig. 4.14(d) as the Re is 458. The wake is chaotic, however, no vortex-ring is found and the vortex street is obvious. The wake is not attached to the sphere up to the Re is 1,720 (see Fig. 4.14(e)-(f)). The flow pattern is similar to the one mentioned in section 4.1.2, which the sphere is without blowing.

4.2.3 Critical Velocity U_{in} for Both Kinds of Burners

Several of fixed V_w are selected to carry out the same experiments as above for the cylindrical and spherical burners. The critical incoming flow velocity U_{in} , above which the wake starts to return to the rear of burner, as a function of V_w is shown in Table 4.3. Based on the present data, the demarcation lines for three burners are plotted in Fig. 4.15. For the case of 15mm-diameter cylinder, the boundary for the wake between blow-off from and return to the rear surface of burner can be correlated as:

$$U_{in} = -1.8886 + 1.6119 \times V_w \quad (4-1)$$

Similarly, the correlation for 20mm-diameter cylinder is

$$U_{in} = -1.4299 + 1.7036 \times V_w \quad (4-2)$$

The case for the 15mm-diameter sphere is also dealt with the same manner and the correlation is

$$U_{in} = -0.1981 + 0.4459 \times V_w \quad (4-3)$$

These three correlation lines are also shown in Fig. 4.15.

The results in this plot manifest that the critical U_{in} is almost linearly varied with V_w no matter what the burner shapes in this thesis. However, it is apparent that the trend of the critical U_{in} 's exhibits:

U_{in} cylinder (20mm) > U_{in} cylinder (15mm) > U_{in} sphere (15mm)
 under a fixed V_w , greater than 1.5 cm/s. It may be attributed to that under a fixed V_w , the ejection volumetric flow rate of 20mm-diameter cylinder is greater than the others because of its greater surface area. The greater ejection rate leads to a greater static pressure around the surface of the burner. It also can be seen that the slopes of the Eq. (4-1) and the Eq. (4-2) are almost the same. Therefore, a region map is replotted in Fig. 4.16 in terms of the parameters, chosen as $V_w(D/L)$ and $U_{in}(D/L)^{0.5}$, where D is the diameter and L the length of the cylinder. The boundary for the wake between blow-off from and return to the rear surface of burner independent of burner's diameter can be correlated as

$$U_{in} \left(\frac{D}{L} \right)^{0.5} = -0.1549 + 1.6447 \times \left[V_w \left(\frac{D}{L} \right) \right]^2 \quad (4-4)$$

The correlation is also shown in Fig. 4.16 and its application is discussed in detail in the next section.

4.3 Comparisons with Chang's [2] and Tsa's [1] Studies

The size of the cylindrical burner used in Chang [2] is different from the ones used in this study. Therefore, the Eq. (4-4) is employed to deduce the V_w and the critical U_{in} for the size of cylinder in Chang [2]. The diameter of cylinder used in Chang [2] is 30mm and its length of 40mm is the same as the one used in this study. The results of the deduction are shown in Table 4.4. The U_{in} , above which the lift-off flame is drawn back to become a wake flame again, and the corresponding V_w observed by Chang [2] are also shown in Table 4.4. According to the data in Table 4.4, a configuration map is shown in Fig. 4.17 in terms of the parameters chosen as the V_w and the critical U_{in} . The cold flow structures can be corresponded to the resultant flame behaviors mentioned in Chang [2], which the lift-off flame is transformed into second wake flame, with the same Re . In Fig. 4.17, for the case of cold flow structures, the trend for the variation of the critical U_{in} with the increasing V_w is almost linear, and the left side of region map infers the wake is return to the rear of burner. However, since the flow in combustion involves many complicated factors as mentioned in Chang [2], it can be seen that V_w barely influences the mechanism of the lift-off flame transformed into second wake flame. The resultant cold flow visualizations in this thesis just provide a part of assistance to realize the physical mechanism for the occurrence of the second wake flame in Chang [2]. Besides, Tsa [1] found that a larger fuel-ejection area gives a wider flame lift-off incoming flow velocity range. It is confirmed in this thesis that the bigger cylinder with the greater critical U_{in} under a fixed V_w .

CHAPTER 5

CONCLUSIONS AND SUGGESTIONS

The cold flow visualizations for flow over the cylindrical and spherical burners have been carried out in this thesis. The basic experimental apparatuses in the present study is the same as those of Chang's [2], which are the wind tunnel, the porous sintered burners and the measurement instrumentations. However, the test section of wind tunnel is modified to install the smoke-generator wire and laser-sheet lighting, which are used to visualize the cold flow behaviors.

The investigation consists of two parts. The first one is to visualize the flow field around and behind the cylindrical and spherical burners without air blowing. The range of Re for the cases of 15mm-diameter cylinder and the sphere is from 143 to 2,092 and those are from 191 to 2,356 for the 20mm-diameter cylinder. The purpose of the first part is to confirm the experimental accuracy, and the observed flow behaviors are confirmed by the relative literature. For instance, the flow patterns shown in Fig. 4.2(b) ($Re = 210$) and Fig. 4.2(h) ($Re = 2,092$) are quite similar to those in Figs. 4.5 and 4.6, respectively, obtained by Koopmann ($Re = 200$) and Wérle and Gallon ($Re = 2,000$) in an album of fluid motion [31].

The second part is to investigate the effect of the blowing from burner on the flow behaviors. Under the various air ejection velocities (V_w), the resultant flow patterns for cylindrical and spherical burners associated with varying Re are visualized. For the case of 15mm-diameter cylinder, V_w is specified at 1.76 cm/s. It is found that as Re approaches to

907, the wake returns to the rear of cylinder and it seems to have no ejection from the cylinder. It may be attributed to that once the static pressure of the downstream wake is greater than the one caused by the blowing over the surface of the cylinder, the wake is pressed back to the rear of cylinder. Furthermore, several V_w are selected to carry out the similar experiments, and a correlation between V_w and the critical U_{in} , above which the wake returns to the rear of burner, is obtained. The correlation is

$$U_{in} = -1.8886 + 1.6119 \times V_w.$$

For the 20mm-diameter cylinder, under the specified V_w of 1.32 cm/s, the critical U_{in} is found as Re approaches to 1,057. The flow behaviors for the 20mm-diameter cylinder are similar to those for the 15mm-diameter one mentioned previously. It also correlated V_w and the critical U_{in} with

$$U_{in} = -1.4299 + 1.7036 \times V_w.$$

Finally, the boundary for the wake between blow-off from and return to the rear surface of cylinder burner independent of its diameter can be correlated as

$$U_{in} \left(\frac{D}{L} \right)^{0.5} = -0.1549 + 1.6447 \times \left[V_w \left(\frac{D}{L} \right) \right]^2.$$

The phenomenon of the wake returns to the rear of burner is also observed for the case of the sphere. V_w is set at 4.72 cm/s and the wake is not attached to the sphere until Re is 1,720. Similarly, the correlation between V_w and the critical U_{in} is

$$U_{in} = -0.1981 + 0.4459 \times V_w.$$

The cold flow structures can be corresponded to the resultant flame

behaviors, which the lift-off flame is transformed into second wake flame, with the same Re . Although the reacting flow of combustion involves many complicated factors, the cold flow visualization gives a partial assistance to realize the physical mechanism for the occurrence of the second wake flame.

Finally, there are some suggestions for extending the present experiment. It is worthy to change the material of the burner to acrylics, which it is transparent to make the visualization more easily. The dual porous cylinders would be inserted into the test section to study the flow interference patterns. Moreover, the rear part of test section would be modified to the one that is easy to build and take apart so that the cold flow visualization and combustion experiments can be carried out alternatively. For example, it could employ the acrylics to form the rear side of test section as the flow visualization is proceeding. Then, the side view of the flow patterns would be observed and the three-dimensional phenomena and aspects would be further comprehended.

References

1. S. S. Tsa, Mutual Interaction between Counterflow Flames over Binary Tsuji Burners in Side-by-Side Arrangement, Ph. D. Dissertation, National Chiao Tung University, Taiwan, 2003.
2. C. C. Chang, Experimental Visualization of Counterflow Diffusion Flame over a Porous Cylinder, M. S. thesis, National Chiao Tung University, Taiwan, 2002.
3. J. Y. Wang, The Effect of Interaction Between Two Porous Flame Mechanism With Nitrogen Ejector, M. S. Thesis, National Taiwan University, Taiwan, 1998.
4. C. H. Chen and F. B. Weng, Flame Stabilization and Blowoff Over a Porous Cylinder, *Combustion Science and Technology*, vol. 73, pp. 427-446, 1990.
5. K. Wohl, N. Kapp, and C. Gazley, The Stability of Open Flames, *Third Symposium on Combustion Flame and Explosion Phenomena*, pp. 3-21, 1949.
6. S. Taneda, Experimental Investigation of the Wake Behind a Sphere at Low Reynolds Numbers, *J. Phys. Soc. Japan*, 11, pp. 1104-1108, 1956.
7. R. Natarajan and A. Acrivos, The Instability of the Steady Flow Past Spheres and Disks, *Journal of Fluid Mechanics*, 254, pp. 323-344, 1993.
8. E. Achembach, Vortex Shedding from Spheres, *Journal of Fluid Mechanics*, 62, pp. 209-221, 1974.
9. H. Sakamoto and H. Haniu, A Study on vortex Shedding from Spheres in a Uniform Flow. *Trans. ASME: J. Fluids Engng*, 112, pp. 386-392, 1990.
10. A. G. Tomboulides, S. A. Orszag, and G. E. Karniadakis, Direct and Large-eddy Simulation of Axisymmetric Wakes, *AIAA Paper*, 93-0546, 1993.
11. T. A. Johnson and V. C. Patel, Flow Past a Sphere up to a Reynolds Number of 300, *Journal of Fluid Mechanics*, 378, pp. 19-70, 1999.
12. D. J. Tritton, Experiments on the Flow past a Circular Cylinder at Low Reynolds Numbers, *Journal of Fluid Mechanics*, 6, pp. 547-567, 1959.
13. J. H. Gerrard, The Wakes of Cylindrical Bluff Bodies at Low Reynolds Number, *Journal of Fluid Mechanics*, 25, pp. 401-413,

- 1966.
- 14.M. M. Zdravkovich, Smoke Observations of the Formation of a Kármán Vortex Street, *Journal of Fluid Mechanics*, 37, pp. 491-496, 1969.
 - 15.A. E. Perry, M. S. Chong and T. T. Lim, The Vortex-shedding Process behind Two-dimensional Bluff Bodies, *Journal of Fluid Mechanics*, 116, pp. 77-90, 1982.
 - 16.R. B. Green and J. H. Gerrard, An Optical Interferometric Study of the Wake of a Bluff Body, *Journal of Fluid Mechanics*, 226, pp. 219-242, 1991.
 - 17.L. Mathelin, F. Bataille and A. Lallemand, Near Wake of a Circular Cylinder Submitted to Blowing-I Boundary Layers Evolution, *International Journal of Heat and Mass Transfer*, 44, pp. 3701-3708, 2001.
 - 18.L. Mathelin, F. Bataille and A. Lallemand, Near Wake of a Circular Cylinder Submitted to Blowing-II Impact on the Dynamics, *International Journal of Heat and Mass Transfer*, 44, pp. 3709-3719, 2001.
 - 19.H. Q. Zhang, U. Fey and B. R. Noack, On the Transition of the Cylinder Wake, *Physics of Fluids*, 7, pp. 779-794, 1995.
 - 20.M. Brede, H. Eckelmann and D. Rockwell, On Secondary Vortices in the Cylinder Wake, *Physics of Fluids*, 8, pp. 2117-2124, 1996.
 - 21.Y. Yokoi and K. Kamemoto, Initial Stage of a Three-dimensional Vortex Structure Existing in a Two-dimensional Boundary Layer Separation Flow (Visual Observation of Laminar Boundary Layer Separation over a Circular Cylinder from the Side of a Separated Region), *JSME*, 36, 201-206, 1993.
 - 22.N. Fukamachi, Y. Ohya, and Y. Nakamura, Improvement of The Smoke-wire Method of Flow Visualization, *Fluid Dynamics Research*, 7, pp. 23-29, 1991.
 - 23.T. J. Mueller, Recent Developments in Smoke Flow Visualization, Hemisphere Publ Corp, pp. 30-40, 1985.
 - 24.A. J. Smith and T. T. Lim, Flow Visualization: Techniques and Examples, Imperial College Press, pp. 54-61, 2000.
 - 25.J. C. Yang, M. K. Donnelly, N. C. Prive, and W. L. Grosshandler, Dispersed Liquid Agent Fire Suppression Screen Apparatus, NISTIR 6319, *National Institute of Standards and Technology*, 1999.
 - 26.Laboratory Methods of Testing Fans for Rating, ANSI/AMCA 210-85

- Standard, 1985.
- 27.V. R. Chen, Experimental Visualization and Measurements for Flame Interaction Between Dual Tsuji Burners in Side-by-Side Arrangement, M. S. thesis, National Chiao Tung University, Taiwan, 2003.
- 28.R. W. Fox, and A. T. McDonald, Introduction to Fluid Mechanics, John Wiley and Sons, Canada, 1994.
- 29.S. J. Kline, and F. McClintock, Describing Uncertainties in Single-Sample Experiments, *Mechanical Engineering*, vol. 75, pp. 3-8, 1953.
- 30.R. J. Moffat, Contributions to the Theory of Single-Sample Uncertainty Analysis, *Journal of Fluid Engineering*, vol. 104, pp. 250-260, 1982.
- 31.V. D. Milton, An Album of Fluid Motion, THE PARABOLIC PRESS, Stanford, California, 1982.

